Metallopeptide Based Mimics With Substituted Histidines Approximate a Key Hydrogen Bonding Network in the Metalloenzyme Nickel Superoxide Dismutase

Jason Shearer[*], **Kosh P. Neupane**, and **Paige E. Callan**
Department of Chemistry, University of Nevada, Reno, NV 89557

Abstract

Nickel superoxide dismutase (NiSOD) is a recently discovered superoxide dismutase that utilizes the Ni^{III}/Ni^{II} couple to facilitate the disproportionation of $O_2^{\bullet-}$ into H_2O_2 and O_2. A key structural component of NiSOD is an elongated axial His-imidazole Ni^{III} bond (2.3 – 2.6 Å) that is the result of a H-bonding network between His(1), Glu(17), and Arg(47). Herein we utilize metallopeptide based mimics of NiSOD with His(1) ε-nitrogen substituted imidazoles to approximate the electronic influence of this H-bonding network ($\{Ni^{III/II}(SOD^{M1}–Im–X)\}$ X = Me, H, DNP, and Tos; $SOD^{M1}–Im–X$ = H′CDLPCGVYDPA where H′ is an *N*-substituted His). All reduced $\{Ni^{II}(SOD^{M1}–Im–X)\}$ are similar to one another as assessed by electronic absorption spectroscopy, CD spectroscopy, and Ni K-edge XAS. This indicates that the change in His(1) is having little influence on the square-planer $Ni^{II}N_2S_2$ center. In contrast, changes to the axial His(1) ligand impart differential spectroscopic properties on the oxidized $\{Ni^{III}(SOD^{M1}–Im–X)\}$ metallopeptides. Resonance Raman spectroscopy (405 nm excitation) in conjunction with a normal coordinate analysis indicates that as the axial His imidazole is made less Lewis basic there is an increase in $Ni^{III}–S$ bond strength in the equatorial plane, with force constants for the Ni-S bond *trans* to the amine ranging from 1.54 to 1.70 mdyn Å^{-1}. The rhombic EPR spectra of the four oxidized metallopeptides are all consistent with low-spin Ni^{III} contained in a square pyramidal coordination environment, but show changes in the hyperfine coupling to ^{14}N along g_z. This is attributable to a reorientation of the g_z vector in the more (along the $Ni^{III}–N^{imidazole}$ bond) *vs.* less (along the $S–Ni^{III}–N^{amine}$ bond) Lewis basic imidazole bases. This reorientation of g_z along the xy plane translates into a decrease in A_{zz} by ~20 MHz. A decrease in Lewis-basicity of the axial imidazole also translates into a two order of magnitude *increase* in SOD catalysis across the metallopeptide series, with k_{cat} ranging from $6(1) \times 10^6$ M^{-1} s^{-1} for the metallopeptide with the most Lewis basic imidazole to $6(2) \times 10^8$ M^{-1} s^{-1} for the metallopeptide with the least basic imidazole. This likely results from a fine tuning of the electron transfer properties of the Ni-center, which optimize it for SOD catalysis.

Superoxide ($O_2^{\bullet-}$) is a toxic byproduct of anaerobic respiration, and its cellular degradation is typically catalyzed by redox-active metalloenzymes called superoxide dismutases (SODs).[1–4] SODs facilitate the degradation of $O_2^{\bullet-}$ by catalyzing its disproportionation into H_2O_2 and O_2:

$$SOD^{red} + O_2^{\bullet-} + 2H^+ \rightarrow SOD^{ox} + H_2O_2 \qquad (1)$$

Corresponding author's: shearer@unr.edu.

$$SOD^{ox} + O_2{}^{\bullet-} \rightarrow SOD^{red} + O_2 \qquad (2)$$

and fall into one of four classes (Cu/ZnSOD,[5] FeSOD,[6,7] MnSOD,[6,7] and NiSOD[8]) based on the metal cofactor(s) found at their active-site. Nickel containing superoxide dismutase (NiSOD) is the most recently discovered SOD, and was first found in several *Streptomyces* species and cyanobacteria.[9−12] A more recent bioinformatics study has demonstrated that the gene encoding for NiSOD is found in several aquatic bacteria and invertebrates.[13]

NiSOD exists as a homohexamer in solution with each monomer containing one mononuclear Ni-ion. The nickel center is ligated within a loop comprised of residues 1 – 6 from the *N*-terminus (the "nickel binding hook").[14−16] In the reduced Ni^{II} oxidation state the nickel center is found in a square planar N_2S_2 coordination environment with two *cis*-cysteinate ligands from Cys(2) and Cys(6), the *N*-terminal amine from His(1), and the amidate nitrogen from Cys(2) (Scheme 1). Upon oxidation to Ni^{III}, the imidazole δ-nitrogen from His(1) will coordinate to the nickel ion in an axial position forming a square-pyramidal geometry about nickel (Scheme 1).

X-ray crystallographic analysis of oxidized NiSOD shows that the axial Ni–N bond is substantially elongated compared to "typical" Ni^{III}-N bonds with neutral N-donors; in NiSOD this bond is greater than 2.3 Å long, compared to ~2.0 Å long for a typical Ni^{III}-N bond.[17−21] Brunold and coworkers have suggested that this elongated Ni-N bond is due to a hydrogen bonding network between the ε N-H group of His(1) and Glu(17) and Arg(47) on an adjacent protein monomer.[17] Density functional theory (DFT) and hybrid-DFT calculations of computational models of the NiSOD active site show that when the hydrogen bonding network is omitted from the model a normal Ni-imidazole bond length of ~2.0 Å is obtained.[17,18,22] In contrast, inclusion of the outersphere hydrogen bonding interaction to the ε N-H group elongates the Ni-imidazole bond to 2.17 Å.[17] This strongly suggests that the hydrogen bonding network is at least partially responsible for the increase in Ni-imidazole bond length; the H-bonding network is structurally constraining the imidazole in a position relatively far-removed from the Ni-center. Thus, from the standpoint of the Ni-center, it is being presented with a less Lewis-basic donor. It seems highly likely that this alteration of the axial Ni^{III}–N bond length will have an influence on the physical and reactivity properties of the metalloenzyme when compared to similar Ni-centers where this Ni-N bond would be at a typical length.

We and others have successfully modeled many of the structural, spectroscopic, and functional properties of NiSOD using small metallopeptide based biomimetic compounds containing the first seven to twelve residues from the N-terminal sequence of *S. coelicolor* NiSOD.[18,23−26] In one of these studies we found that the inclusion of an amino acid residue that has the potential to coordinate Ni in the axial position greatly enhances the SOD activity of the resulting metallopeptide.[18] If the *N*-terminal histidine was replaced with alanine the activity of the resulting metallopeptide dropped by over an order of magnitude. In contrast, the replacement of the *N*-terminal histidine with glutamic acid afforded a metallopeptide with only a modest reduction in SOD activity. This is in line with mutation studies performed by Maroney and coworkers who have shown that mutation of His(1) to a residue with a non-coordinating side-chain all but eliminated SOD activity in the metalloenzyme.[27]

Incorporation of intricate outer-sphere interactions found in metalloproteins is difficult to accomplish using metallopeptide based mimics. Furthermore, changing these interactions in a systematic and predictable manner in metallopeptide based mimics is nearly impossible. Therefore, to more finely probe the role that the axial ligand to Ni^{III} has in controlling the activity of the metalloenzyme NiSOD we have prepared a series of metallopeptides ({Ni

(SOD^{M1}–Im-X)}; SOD^{M1}–Im-X = H$_2$N-H′CDLPCGVYDPA-COOH and H′ is an *N*–substituted imidazole) that have variable *N*-substitution of the His(1) imidazole ε-nitrogen (Chart 1). The resulting *N*-substituted imidazoles will impart changes to the electron donating ability of the imidazole δ-nitrogen, making it a more or less Lewis-basic donor to the Ni^{III} center. Although changing the electronics of the imidazole donor cannot account for all of the fine-tuning provided by the protein environment, it will be shown that this one subtle change is capable of reproducing a number of the key aspects of the electronic and reactivity properties of the metalloenzyme. In fact, we will demonstrate that *weakening* the axial N-Ni^{III} bond through these subtle electronic changes to the axial imidazole ligand enhances SOD activity and makes the resulting metallopeptide-based mimic more NiSOD-like. Possible reasons for these findings will be discussed.

Experimental Section

Preparation of {Ni^{II}SOD^{M1}H(1)X}

SOD^{M1}–Im–X (H$_2$N-H′CDLPCGVYDPA-COOH; H′ = H, H^{Me}, H^{Tos}, H^{DNP}) were prepared by manual solid phase peptide synthesis on Wang resin using Fmoc/^{t}Bu protecting groups in a manner similar to what has been previously described,[24] except for SOD^{M1}–Im–DNP, which was synthesized using HMPB-BHA resin. Fmoc-protected $^\varepsilon$*N*-methyl histidine (H^{Me}) was obtained from Bachem (Torrance, CA), while $^\varepsilon$*N*-tosyl histidine (H^{Tos}) and $^\varepsilon$*N*-2,4-dinitrophenyl histidine (H^{DNP}) were purchased from Advanced ChemTech (Louisville, KY). The peptides were cleaved from the resin using 95% TFA/2.5% ethanedithiol/2.5% triisopropyl silane (95% TFA/5% triisopropyl silane for SOD^{M1}–Im–DNP), and the cleavage solution was evaporated under vacuum to dryness. The glassy crude product was washed with peroxide-free diethyl ether, and the peptides were purified by reverse phase HPLC on a Waters X-terra C-18 column (semi-preparative: 5 μm 50 × 100 mm; analytical: 5 μm 4.6 × 100 mm) and lyophilized yielding white powders (yellow for SOD^{M1}H(1)H^{DNP}).

SOD^{M1}–Im–Me

R_t = 15.6 min (analytical: 10 – 65% MeCN/Water 0.1% TFA over 45 min), R_t = 3.4 min (semi-preparative: 10 – 29% MeCN/Water 0.1% TFA over 15 min). ESI-MS (positive ion mode) M$^+$ *m/z*: cacld. 1303.4; found 1303.3. Yield: 132 mg (56%).

SOD^{M1}–Im–Tos

R_t = 22.4 min (analytical: 10 – 65% MeCN/Water 0.1% TFA over 45 min), R_t = 3.8 min (semi-preparative: 10 – 29% MeCN/Water 0.1% TFA over 15 min). ESI-MS (positive ion mode) M$^+$ *m/z*: cacld. 1443.4; found 1443.8. Yield: 35 mg (14%).

SOD^{M1}–Im–DNP

R_t = 19.3 min (analytical: 10 – 65% MeCN/Water 0.1% TFA over 45 min), R_t = 18.0 min (semi-preparative: 10 – 30% MeOH/Water 0.1% TFA over 25 min). ESI-MS (positive ion mode) M$^+$ *m/z*: cacld. 1455.4; found 1455.3. Yield: 60 mg (21%).

Under a dinitrogen atmosphere in a glove bag (or a 3:97 H$_2$:N$_2$ mixed atmosphere in a COY anaerobic chamber) solutions of the peptides were then prepared in 50 mM NEM buffer (pH = 7.4). The peptide concentrations of these solutions were determined by the methods of Ellman.[28] To these peptide solutions 1 eq. of NiCl$_2$ dissolved in water (pH = 7.4) was added affording the reduced Ni^{II} metallopeptides.

{Ni^{II}(SOD^{M1}–Im–Me)}

Electronic absorption spectrum λ_{max} (cm^{-1}) (ε (M^{-1} cm^{-1})): 27,400 (940); 21,690 (360); 18,050 (160, sh). ESI-MS (positive ion mode) M$^+$ *m/z*: cacld. 1359.1; found 1358.3.

{Ni^{II}(SOD^{M1}–Im–Tos)}

Electronic absorption spectrum λ_{max} (cm^{-1}) (ε (M^{-1} cm^{-1})): 21,730 (405, sh); 18,110 (180, sh). ESI-MS (positive ion mode) M$^+$ *m/z*: cacld. 1499.1; found 1498.9.

{Ni^{II}(SOD^{M1}–Im–DNP)}

Electronic absorption spectrum λ_{max} (cm^{-1}) (ε (M^{-1} cm^{-1})): 38,127 (25,700), 29,130 (5,590), 21,560 (410, sh), 18,110 (150, sh). ESI-MS (positive ion mode) M$^+$ *m/z*: cacld. 1511.1; found 1510.8.

Preparation of {Ni^{III}(SOD^{M1}–Im–Me)}

In a COY anaerobic chamber a ~1 – 3 mM solution of {Ni^{II}(SOD^{M1}–Im–Me)} was prepared in 50 mM NEM buffer (pH = 7.4) and placed on an ice bath. To this 0.51 eq. of I$_2$ in ethanol was added slowly dropwise. Over the course of the addition, the solution changed from a light pink/beige to dark orange/brown. This solution was then used as prepared. Alternatively, {Ni^{III}(SOD^{M1}–Im–Me)} could be prepared from the addition of 1.0 eq. of KMnO$_4$ in substitution of 0.51 eq. of I$_2$ followed by dialysis of the solution against 50 mM NEM buffer (pH 7.4) to remove all Mn compounds from solution. All GPC data for oxidized {Ni^{III}(SOD^{M1}–Im–Me)} were collected using a Waters Protein-Pak^{TM} GPC column (7.8 × 300 mm; 60 Å pore size) using a saturated NaHCO$_3$ mobile phase (pH 8.3). GPC traces were monitored at 350 nm where the free SOD^{M1}–Im–Me peptide does not absorb. Electronic absorption spectrum λ_{max} (cm^{-1}) (ε (M^{-1} cm^{-1})): 28,575 (3,260); 25,575 (sh); 18,210 (740). EPR (77 K 1:1 NEM buffer:glycerol): g_x = 2.33; g_y = 2.24; g_z = 2.00 (A$_{zz}$ = 84 MHz). ESI-MS (positive ion mode) M$^+$ *m/z*: cacld. 1359.1; found 1359.2.

Stopped-Flow Kinetic Studies

A HI-TECH SF-61 stopped flow kinetics instrument equipped with double mixing syringes was utilized for the measurement of the catalytic O$_2$$^{\bullet-}$ disproportionation reactions facilitated by {Ni(SOD^{M1}–Im–X)}. One of the 2.5 mL syringes was filled with buffer (50 mM NEM pH 8.0). The second 2.5 mL syringe was filled with a solution of {Ni$^{II/III}$(SOD^{M1}–Im–X)} (final mixing concentrations ranging from 1.0 – 60 μM). A third 0.5 mL (or 2.5 mL) syringe was filled with dry DMSO, 18-crown-6 and KO$_2$ (final concentrations ranging between 2.5 – 50 mM). Thus, mixing of the three solutions results in a 10:1 ratio (or 2:1) of buffer:DMSO, which substantially minimizes any optical disturbances from the mixing of the water and DMSO at the beginning of the kinetics run[29,30] (the first 5 ms were disregarded in the kinetic treatment due to such a disturbance). The disappearance of KO$_2$ was subsequently monitored by measuring the change in absorbance at 245 nm as a function of time (ε ~ 2250 M^{-1} cm^{-1}).[29] All kinetics studies were performed at 24.5(5) °C. Prior to all kinetic experiments, several shots of buffer and 18-crown-6/DMSO (or buffer, {Ni^{II}(SOD^{M1}–Im–X)}, and 18-crown-6/DMSO) were recorded and averaged together to use as the base-line. As a test reaction the catalytic O$_2$$^{\bullet-}$ disproportionation afforded by Cu/Zn SOD (from bovine erythrocytes; Sigma Cat. Number S2515) was recorded indicating that we can observe the tail-end of catalytic O$_2$$^{\bullet-}$ disproportion reactions with a rate constant of ~2 × 10^9 M^{-1} s^{-1}.[31] All data work-up and the subsequent rate constants were then extracted from the data using in-house designed procedures for the software package Igor Pro 6.02 (Wavemetrics; Lake Oswego, OR).

Physical Methods

Electronic absorption spectra were obtained on a CARY 50 UV-Vis-NIR spectrophotometer in quartz cells with 1 cm pathlengths. CD spectra were also recorded in quartz cells with 1 cm pathlengths, and were obtained on an OLIS-DCM 17 spectropolarimeter using photomultiplier detectors in the visible region (300 – 700 nm) and InGaAs detectors in the NIR region (600 – 1000 nm). All CD data-sets were averaged together in the overlapping spectral regions.

Electrochemical data were obtained on a Princeton Applied Research PARSTAT 2273 potentiostat using a standard three-electrode cell (pyrolytic graphite edge working electrode, Pt disk auxiliary electrode, SCE reference electrode). Concentrations of $\{Ni^{II}(SOD^{M1}-Im-X)\}$ in 50 mM NEM buffer were ~0.7 – 1.0 mM, and NaCl was used as the supporting electrolyte (100 mM). The solutions were sparged with Ar prior to recording the data. Square wave voltammograms were recorded with a pulse height of 15 mV at a frequency of 5 Hz. The oxidation and reduction waves were then extracted from the background capacitance by applying a cubic spline function before and after the oxidation/reduction peaks. Peak positions were then determined by taking the first derivatives of these data.

EPR spectra were recorded using ~0.05 mM solutions of $\{Ni^{III}(SOD^{M1}-Im-X)\}$ (generated by the addition of 0.5 eq. of I_2 in EtOH) as 1:1 mixtures of buffer:glycerol (buffer = 50 mM NEM pH 7.4) in quartz EPR tubes. The spectra were recorded at 77 K in a quartz EPR finger dewar on a Varian E4 EPR spectrometer interfaced to a PC through a Scientific Software Services EWWIN system. Data were averaged over 40 scans. The following experimental parameters were used: microwave frequency = 9.07 – 9.12 GHz; microwave power = 2.5 – 5.0 mW; modulation amplitude = 10 G; time constant = 10 ms; conversion time = 10 ms; gain = 2×10^4.

Resonance Raman data were obtained using a modified Jobin Yvon U1000 high resolution double monochromator employing 1800 groves/mm gratings and a PMT detector. The gratings were driven by a microstepper motor (50 nm/step resolution) attached to the cosecant bar, and the output from the PMT was recorded using a DATAQ DI-158 data acquisition module. The microstepper motor and data acquisition module were controlled by a PC using in-house written software in C++. The monochromator was calibrated using the Hg emission lines from a low-pressure Hg(Ar) lamp. Excitations were provided with a 405 nm solid state diode laser (band-width ~5 nm) provided by Opto Engine LLC with ~30 mW of laser power at the sample. The light from the laser was passed through a monochromator containing a 2400 grooves/mm holographic grating (for selecting λ_{ex} = 405.0 nm) and then focused onto the sample. Data were collected at room temperature in quartz fluorescence cuvettes or in NMR tubes in a quartz EPR finger dewar at 77 K using a 135° backscattering geometry. Samples were recorded in 1:1 mixtures of buffer:glycerol with concentrations ranging between 1 – 5 mM. All Ni^{III} species were generated by adding concentrated I_2 dissolved in EtOH to the reduced Ni^{II} metallopeptides. All spectra were independently calibrated by using an internal standard of acetaminophen. Force constants were obtained initially from DFT calculations (*vide infra*) and then subsequently refined using the Quantum Chemistry Assisted Normal Coordinate Analysis (QCA-NCA) procedure of Lehnert and Tuczek.[32]

Ni K-edge X-ray absorption data were collected on beamline X3b at the National Synchrotron Light Source (Brookhaven National Laboratories; Upton, NY) as previously described.[24] Samples of ~0.7 – 3 mM of $\{Ni^{III/II}(SOD^{M1}-Im-X)\}$ (50 mM NEM buffer, pH 7.4) were injected between windows made from Kapton tape in aluminum sample holders, and quickly frozen in liquid nitrogen. All spectra represent the average of five to ten data-sets. Data were analyzed using the software packages EXAFS123[33] and FEFF 8.2[34,35] as previously described. All refinements are based on Fourier Filtered $k^3(\chi)$ data over the energy range of k = 2.0 – 12.5 $Å^{-1}$ and back-transformed from r' = 1.0 – 2.5 Å.

Electronic Structure, Excited State, and EPR Calculations

All electronic structure calculations were performed using Neese's software package ORCA version 2.6.35.[36] Geometry optimized (GO) structures were generated from minimized NiSOD active-sites on oxidized forms, and used convergence criteria (in au) of: root-mean-square (rms) and maximum forces 0.0003 and 0.0001, respectively, and rms and maximum gradients of 0.002 and 0.001, respectively. The group attached to the N(ε) of the His(1) imidazole ring was varied between Me (Ni^{III}(SOD^{Me})), H (Ni^{III}(SOD^{H})), 2,4 dinitrophenyl (Ni^{III}(SOD^{DNP})), and –SO$_2$H (Ni^{III}(SOD^{Tos})). GO calculation on all species utilized the local density approximation of Vosko, Wilk, and Nusair,[37] the gradient correction of Becke[38–40] and Perdew[41,42] (BP86/VWN), the TZVP[43–45] for all non-ligating atoms and the aug-TZVPP[43–47] basis set for Ni, S, and all ligating N atoms.

Frequency calculations on all GO structures were performed using the Becke's three parameter hybrid functional for exchange with the Lee-Yang-Parr functional for correlation (the B3LYP hybrid functional),[48,49] two sided displacements, the TZVP[43–45] for all non-ligating atoms, the aug-TZVPP[43–47] basis set for Ni, S, and all ligating N atoms, a 434 point Lebedev angular mesh, and convergence criteria of 10^{-7} E$_h$ in energy. In addition, vibrational frequencies were also obtained using Gaussian 03[50] for Ni^{III}SOD^{Me}, Ni^{III}SOD^{DNP}, Ni^{III}SOD^{Tos} to provide input-files for Lehnert's program for performing the QCA–NCA.[32,51–53] As these calculations were to provide for an initial set of force constants as input for the QCA–NCA programs, we utilized the BP86/VWN functional[38–42] and TZVP basis set on all atoms.[43–45]

EPR g-values and superhyperfine coupling constants were calculated by solving the coupled-perturbed SCF (CP-SCF) equations.[54,55] These calculations utilized the B3LYP functional,[48,49] the TZVP[43–45] basis-set for all non-ligating atoms, the aug-TZVPP[43–47] basis set for Ni and S, and Kutzelnigg's NMR/EPR basis set (IGLO-III) for all ligating N atoms.[56] All orbitals from –100 to 100 E$_h$ of the HOMO/LUMO gap were considered for the EPR calculations, with the center of electronic charge defined as the origin of the g-matrix.

Results and Discussion

We have previously reported on the synthesis and properties of the NiSOD metallopeptide-based mimic {Ni^{II}(SOD^{M1}–Im–H)} (SOD^{M1}: H$_2$N-HCDLPCGVYDPA-COOH).[24] Briefly, the peptide SOD^{M1} was prepared by standard Fmoc based solid-phase peptide synthesis. Upon the addition of one equivalent of NiCl$_2$ to a slightly basic (pH 7.4; 50 mM in N-ethylmorpholine (NEM) or phosphate buffer) solution of SOD^{M1} the metallopeptide {Ni^{II}(SOD^{M1}–Im–H)} is produced, as signified by a pinkish-beige colored solution. The resulting spectroscopic and structural properties of {Ni^{II}(SOD^{M1}–Im–H)} are reminiscent of reduced NiSOD, and the resulting metallopeptide displays high SOD activity (*vide infra*). Considering the utility of using this and similar mimics to understand some of the properties of NiSOD, it was decided to modify {Ni^{II}(SOD^{M1}–Im–H)} to probe how subtle alterations to the electronics of the imidazole axial ligand to Ni^{III} will influence the reactivity and properties of the NiSOD mimic.

Preparation and Spectroscopic Properties of the Reduced Metallopeptide Based Mimics {Ni^{II}(SOD^{M1}–Im–X)} (X = Me, Tos, DNP)

The other SOD^{M1}–Im–X (X = Me, DNP, Tos) peptides used in this study were prepared by standard solid-phase peptide synthesis. Both SOD^{M1}–Im–Tos and SOD^{M1}–Im–DNP were prepared in low overall yields (less than 25%). In both cases a significant quantity of SOD^{M1} was recovered due to the unavoidable cleavage of the tosyl or 2,4-dinitrophenyl groups from the His(1) imidazole. To avoid the excessive cleavage of the 2,4-dinitrophenyl group from the N-terminal His residue of SOD^{M1}(H(1)H^{DNP}) we removed 1,2-dithiolethane from the cleavage cocktail and replaced it with an equal volume of triisopropyl silane. Failure to

perform this substitution resulted in extremely low yields of $SOD^{M1}(H(1)H^{DNP})$ (less than 1%) due to the thiol-assisted cleavage of the dinitrophenyl protecting group.

The metallopeptides {$Ni^{II}(SOD^{M1}$–Im–X)} were prepared in a manner analogous to that previously described for {$Ni^{II}(SOD^{M1}$–Im–H)}.[24] Solutions of the metallopeptides were prepared in aqueous 50 mM NEM buffer (pH 7.4) and 1 eq. of $NiCl_2$ (in water) was added to solution. Upon the addition of $NiCl_2$, both {$Ni^{II}(SOD^{M1}$–Im–Me)} and {$Ni^{II}(SOD^{M1}$–Im–Tos)} yielded light beige-pink solutions, while {$Ni^{II}(SOD^{M1}$–Im–DNP)} remained mostly yellow in color due to the intense 2,4-dinitrophenyl chromophore.

The electronic absorption spectrum of {$Ni^{II}(SOD^{M1}$–Im–Me)} is reminiscent of that reported for reduced NiSOD ($NiSOD^{red}$; Figure 1 and 2; Table 1); it contains weak transitions in the ligand-field region of the spectrum at 27,400, 21,690, and 18,050 cm^{-1} ($NiSOD^{red}$: ~28,000, 22,000, and 18,000 cm^{-1}).[17] The CD spectrum of {$Ni^{II}(SOD^{M1}$–Im–Me)} also resembles that of $NiSOD^{red}$, with positively signed bands at 17,670 and 30,300 cm^{-1} and a negatively signed band at 22,940 cm^{-1} (Figure 2). {$Ni^{II}(SOD^{M1}$–Im–Tos)} possesses an electronic absorption spectrum that is also reminiscent of $NiSOD^{red}$, except that in the high-energy regions the tosyl group dominates the spectrum (Figure 1, Table 1). In contrast to the other metallopeptides investigated in this study, the ligand-field region of the electronic absorption spectrum of {$Ni^{II}(SOD^{M1}$–Im–DNP)} is obscured by the intense 2,4-dinitrophenyl chromophore (Figure 1, Table 1).

The Ni K-edge X-ray absorption spectra of the three Ni^{II} metallopeptides are consistent with a square planar coordination geometry about Ni^{II}. The XANES spectra (Figure 3, Table 2) all show a prominent pre-edge peak corresponding to Ni(1s) → Ni($4p_z$) transitions at ~8338 eV, which is a characteristic feature of square planar Ni^{II} centers.[57] The EXAFS region (Figure 3, Table 2) of the Ni K-edge spectra are best modeled with Ni contained in an N_2S_2 coordination environment with the average Ni–S bond length being between 2.17 – 2.18 Å and the average Ni–N bond length being ~1.92 Å. These metric parameters compare well with EXAFS data reported for $NiSOD^{red}$,[58] and are nearly identical to what was previously reported by us for {$Ni^{II}(SOD^{M1}$–Im–H)} and other NiSOD metallopeptide based mimics.[13,18,24] It therefore appears that all four metallopeptides reported in this study display nearly identical Ni^{II} structures, and that imidazole substitution is having a minimal influence on the structure of the reduced Ni^{II} metallopeptides. This is to be expected as the His(1) imidazole is not directly involved in coordination to the reduced Ni^{II}-center.

Solution Electrochemical Properties of {Ni(SOD^{M1}–Im–X)}

In a previous report we obtained a redox potential for the Ni^{III}/Ni^{II} couple of {Ni(SOD^{M1}–Im–H)} at 0.70(2) V vs. Ag/Ag^+.[24] This potential was obtained as a thin-film on a microelectrode surface. Although thin-film electrochemistry has proven useful in the studies of many redox active materials, it can sometimes be problematic for gaining insight into *solution* electrochemical properties because differences in the microenvironment provided by the film *vs.* solution can dramatically influence the redox potential and electrode kinetics of the electroactive material.[59–62] This should be especially problematic when applied to small metallopeptides where the redox center is largely solvent exposed. We therefore decided to investigate the electrochemical behavior of all of these metallopeptides by solution electrochemistry as opposed to thin film electrochemistry.

All four metallopeptides yield quasireversible Ni^{III}/Ni^{II} redox couples in solution (Supporting Information). Solutions of {$Ni^{II}(SOD^{M1}$–Im–H)} (1.0 mM in: 50 mM NEM; 100 mM NaCl; pH 7.4) display a Ni^{III}/Ni^{II} redox potential at $E = 434(3)$ mV vs. Ag/Ag^+. This is more in line with the solution electrochemical measurements obtained for NiSOD metallopeptide based mimics in our laboratory.[18] In contrast, {$Ni^{II}(SOD^{M1}$–Im–Me)}, which possesses a more

electron donating imidazole donor, stabilizes the Ni^{III} oxidation state to a greater extent with a redox couple of E = 282(4) mV *vs.* Ag/Ag$^+$. As expected, the less electron donating ligands provide for more positive redox potentials with E = 470(10) and 598(5) mV *vs.* Ag/Ag$^+$ for {Ni^{II}(SOD^{M1}–Im–DNP)} and {Ni^{II}(SOD^{M1}–Im–Tos)}, respectively. We note that all four metallopeptides display relatively large peak to peak separations in their voltammograms (ΔE ~ 250 mV). This is likely due to the imidazole ligands binding to and dissociating from the Ni center during the Ni^{III}/Ni^{II} redox process at these relatively slow (v = 100 mV s^{-1}) scan velocities.[18] Very recently Maroney and coworkers reported that the Ni^{II}/Ni^{III} couple for NiSOD is 290 mV vs. NHE (~91 mV vs. Ag/Ag$^+$).[63] {Ni^{II}(SOD^{M1}–Im–Me)} therefore has the closest redox potential to the Ni^{III}/Ni^{II} couple of NiSOD.

Preparation of {Ni^{II}(SOD^{M1}–Im–Me)} *via* Chemical Oxidation

One reason that {Ni^{II}(SOD^{M1}–Im–Me)} was initially prepared was that we reasoned the additional Lewis-basicity of the *N*-methyl imidazole would aid in the stabilization of the Ni^{III} oxidation state. This was indeed confirmed by our CV measurements, which showed a considerably more negative redox potential for {Ni^{II}(SOD^{M1}–Im–Me)} than the other three metallopeptides investigated (*vide supra*). Thus, attempts were made to generate and isolate the stable {Ni^{III}(SOD^{M1}–Im–Me)} species. As an initial test to determine if the Ni^{III} oxidation state could be generated and stabilized we added a concentrated solution of KMnO$_4$ to buffered solutions of {Ni^{II}(SOD^{M1}–Im–Me)} (pH 7.4; 50 mM NEM). This resulted in an intense red/brown colored solution and an increase in the intensity and number of transitions observed in visible region of the UV/Vis spectrum (Figure 4). After the addition of one equivalent of KMnO$_4$ to solutions of {Ni^{II}(SOD^{M1}–Im–Me)} no further change to the electronic absorption spectrum was noted outside of the changes due solely to excess KMnO$_4$ being present in solution. We should note that although MnO$_4^-$ is a multi-electron oxidation reagent we require one equivalent of permanganate to effect the complete oxidation of the metallopeptide. This is despite the fact that there is sufficient electrochemical driving force to effect further metallopeptide oxidations by some of the reduced Mn-based species that would be present in solution. We are currently probing the mechanism of electron transfer to {Ni^{II}(SOD^{M1}–Im–Me)} to sort this issue out.

Addition of 0.5 equivalents of ascorbate to the fully oxidized nickel-containing metallopeptide resulted in the complete reformation of {Ni^{II}(SOD^{M1}–Im–Me)} (Figure 4, inset). This process could be cycled through at least six times without the observable decomposition of {Ni$^{III/II}$(SOD^{M1}–Im–Me)}. Surprisingly, we observe no metallopeptide decomposition following repeated KMnO$_4$/ascorbate additions by both ESI-MS and GPC (Supporting Information). As a milder oxidizing agent I$_2$ dissolved in EtOH was also investigated for the formation of the {Ni^{III}(SOD^{M1}–Im–Me)}, which yielded similar results as KMnO$_4$. Similarly, no metallopeptide damage is noted from ESI-MS, GPC, and HPLC data following {Ni^{III}(SOD^{M1}–Im–Me)} generation using I$_2$ as an oxidant. Attempts were made to isolate the pure Ni^{III} forms of the other metallopeptides probed in this study, but these all proved to be too unstable to handle above liquid nitrogen temperatures for even brief periods of time (*vide infra*).

The Ni^{III} oxidation state of {Ni^{III}(SOD^{M1}–Im–Me)} was confirmed by X-band EPR spectroscopy. Figure 5 displays the 77 K EPR spectrum of I$_2$ generated {Ni^{III}(SOD^{M1}–Im–Me)}, which is consistent with a low-spin S=1/2 Ni^{III} species. The EPR spectrum is rhombic with g values at g = 2.33, 2.24, and 2.00 (oxidized NiSOD; NiSOD^{ox} has g = 2.30, 2.24, 2.01; Table 3). Furthermore, there is strong superhyperfine coupling in g_z (A_{zz} = 84 MHz), indicative of coupling of the unpaired electron with an ^{14}N nucleus. This coupling is also observed in NiSOD^{ox}, but the superhyperfine coupling constant is considerably smaller in NiSOD^{ox} (A_{zz}

= 69.7 MHz),[9,17,58] indicating that there is a stronger interaction between the unpaired spin on the Ni^{III} center and a nitrogen nucleus in $\{Ni^{III}(SOD^{M1}–Im–Me)\}$ vs. $NiSOD^{ox}$.

The XANES portion of the $\{Ni^{III}(SOD^{M1}–Im–Me)\}$ Ni K-edge X-ray absorption spectrum also shows changes relative to that recorded for $\{Ni^{II}(SOD^{M1}–Im–Me)\}$ that are consistent with a change from the Ni^{II} to Ni^{III} oxidation state (Figure 6; Table 2).[57] The energy of the edge jump shifts by 2.8(6) eV higher in energy in $\{Ni^{III}(SOD^{M1}–Im–Me)\}$ compared with $\{Ni^{II}(SOD^{M1}–Im–Me)\}$. Furthermore, the Ni 1s $\rightarrow$ $4p_z$ transition displayed in $\{Ni^{II}(SOD^{M1}–Im–Me)\}$ now become blurred into the edge of the XANES of $\{Ni^{III}(SOD^{M1}–Im–Me)\}$ while the Ni 1s $\rightarrow$ 3d transition in $\{Ni^{III}(SOD^{M1}–Im–Me)\}$ is considerably more intense than for $\{Ni^{II}(SOD^{M1}–Im–Me)\}$. The increase in intensity of the Ni 1s $\rightarrow$ 3d transition is consistent with both a change in symmetry about the Ni center and an increase in the number of holes in the 3d-manifold. Each of these would be expected with a change from four-coordinate square planar Ni^{II} to five coordinate square pyramidal Ni^{III}; the pseudo-center of inversion would be lost in $\{Ni^{III}(SOD^{M1}–Im–Me)\}$ *vs.* $\{Ni^{II}(SOD^{M1}–Im–Me)\}$, thus the parity forbidden Ni 1s $\rightarrow$ 3d transition gains intensity through a dipole mechanism in a square-pyramidal *vs.* square-planar coordination environment, combined with an increase in the number of final states available to the Ni^{III}-ion.[65,66]

The EXAFS region of the Ni K-edge X-ray absorption spectrum for $\{Ni^{III}(SOD^{M1}–Im–Me)\}$ is consistent with Ni contained in a five coordinate N_3S_2 ligand environments (Figure 6; Table 2). We can best model the EXAFS region with two Ni-S scatterers at 2.19 Å and three Ni-N scatterers at 1.89 Å. These data are nearly identical to what was previously reported by Maroney and co-workers for $NiSOD^{ox}$, and are also consistent with the change in oxidation state and coordination number. The negligible change of the average Ni-S would be expected due to the increase in charge about the Ni-center being offset by the increase in coordination number about Ni from 4 to 5.

The vis-NIR electronic absorption and CD spectra of I_2 generated $\{Ni^{III}(SOD^{M1}–Im–Me)\}$ are displayed in Figure 7 (Table 1). The electronic absorption spectrum is similar to what has been previously reported for $NiSOD^{ox;17}$ it is a relatively broad featureless spectrum from 35,000 – 12,000 cm^{-1} punctuated with a peak at 28,410 cm^{-1} and shoulders at 25,645 and 18,115 cm^{-1}. In contrast to the electronic absorption spectrum of $\{Ni^{III}(SOD^{M1}–Im–Me)\}$, its CD spectrum is distinct from that observed for $NiSOD^{ox}$. The CD spectrum of $\{Ni^{III}(SOD^{M1}–Im–Me)\}$ between 35,000 – 12,000 cm^{-1} is characterized by a positively signed low-energy transition at 13,775 cm^{-1} and a series of negatively signed higher energy transitions between 16,500 – 27,000 cm^{-1}. This can be contrasted with the CD spectrum of $NiSOD^{ox}$, which displays a series of positively and negatively signed features over the energy region of 16,500 – 27,000 cm^{-1} in the CD spectrum.[17] This is likely a manifestation of the differential electronic properties of the Ni-center imparted by weak *vs.* strong axial imidazole donor in $\{Ni^{III}(SOD^{M1}–Im–Me)\}$ vs. $NiSOD^{ox}$.

$\{Ni^{III}(SOD^{M1}–Im–Me)\}$ was probed further by resonance Raman (rR) spectroscopy. Excitation of $\{Ni^{III}(SOD^{M1}–Im–Me)\}$ using 405.0 nm light resulted in a significant enhancement of three Raman active vibrational modes at 323, 343, and 388 cm^{-1} (Figure 8, Table 4). We note that these are due exclusively to the Ni^{III} form of the metallopeptide as excitation of identical concentrations of $\{Ni^{II}(SOD^{M1}–Im–Me)\}$ at 405.0 nm using similar integration times did not lead to a significant signal in this region of the rR spectrum. These resonance enhanced Raman modes are similar as those observed for $NiSOD^{ox}$, and correspond to N-Ni-S stretches.[17,67] It should be noted that the Ni-S vibrational modes observed in $\{Ni^{III}(SOD^{M1}(H(1)H^{Me}))\}$ occur at lower energy than those observed in $NiSOD^{ox}$ ($NiSOD^{ox}$ v_{Ni-S} = 349, 365, and 391 cm^{-1}).[17,67] This reduction in stretching frequency is reflected in the calculated force constants for the Ni–S bonds in $\{Ni^{III}(SOD^{M1}–Im–Me)\}$ *vs.*

NiSOD^{ox}. A normal coordinate analysis (NCA) yields force constants of 1.54 and 1.31 mdyn Å^{-1} for the Ni–S bond *trans* to the amine and *trans* to the amide, respectively. These are significantly reduced when compared to the corresponding force constants of 1.79 and 1.68 mdyn Å^{-1} found in NiSOD^{ox,67} indicating that strong axial coordination by the imidazole is significantly weakening the equatorial Ni–S bonds, as might be expected.

Low Temperature Generation and Trapping of {Ni^{III}(SOD^{M1}–Im–X)} (X = H, DNP, and Tos)

Attempts were made to prepare and isolate the Ni^{III} forms of {Ni^{III}(SOD^{M1}–Im–X)} (X = H, DNP, and Tos) on an ice-bath for detailed study without success. The oxidation of {Ni^{II}(SOD^{M1}–Im–X)} (X = H, DNP, and Tos) by I$_2$, KMnO$_4$, KO$_2$, and Oxone® all yielded intractable polymeric materials. It was possible, however, to generate sufficient quantities of {Ni^{III}(SOD^{M1}–Im–X)} in EPR and NMR tubes at low temperatures (~ –15 °C) in 1:1 buffer:glycerol mixtures (buffer = 50 mM NEM pH 7.4) followed by rapidly freezing the solutions in liquid nitrogen for study by EPR and rR spectroscopy.

For both {Ni^{III}(SOD^{M1}–Im–DNP)} and {Ni^{III}(SOD^{M1}–Im–Tos)} we were able to obtain rR spectra following excitation at 405.0 nm. As the axial imidazole is made less Lewis-basic the resulting N–Ni–S vibrational modes observed in {Ni^{III}(SOD^{M1}–Im–Me)} increase in energy by 8 – 18 cm^{-1} (Figure 8, Table 4). This corresponds to a strengthening of the calculated force constants for the Ni-S bonds. For {Ni^{III}(SOD^{M1}–Im–DNP)} the NCA derived force constants are 1.69 and 1.47 mdyn Å^{-1} for the Ni–S bond *trans* to the amine and *trans* to the amide, respectively. The Ni-S bond of {Ni^{III}(SOD^{M1}–Im–Tos)} are even stronger at 1.70 and 1.51 mdyn Å^{-1}, which are the closest to the strong Ni-S bonds found in NiSOD^{ox} of the oxidized metallopeptides investigated in this study.[67] Warming the solutions to room temperature for several minutes resulted in both the decomposition of the Ni^{III} metallopeptides and the disappearance of the bands attributable to the Ni^{III}–S stretches in both {Ni^{III}(SOD^{M1}–Im–DNP)} and {Ni^{III}(SOD^{M1}–Im–Tos)}. Attempts were made to probe the rR spectrum of {Ni^{III}(SOD^{M1}–Im–H)} without success as excitation of this metallopeptide at 405 nm (and other visible wavelengths) leads to significant photobleaching of the sample.

The EPR spectra of {Ni^{III}(SOD^{M1}–Im–X)} (X = H, DNP, and Tos) are displayed in Figure 5. As can be seen all three EPR spectra are similar in appearance to that obtained for {Ni^{III}(SOD^{M1}–Im–Me)}, including the superhyperfine coupling in g_z, which is indicative of low-spin Ni^{III} with nitrogen coordination along g_z. As the Lewis-basicity of the axial ligand is decreased there is a decrease in A_{zz}. For {Ni^{III}(SOD^{M1}–Im–H)} A_{zz} is equal to 80 MHz, while it decreases to 65 and 67 MHz for {Ni^{III}(SOD^{M1}–Im–DNP)} and {Ni^{III}(SOD^{M1}–Im–Tos)}, respectively. The EPR spectra of the metallopeptides with the weaker imidazole donors ({Ni^{III}(SOD^{M1}–Im–DNP)} and {Ni^{III}(SOD^{M1}–Im–Tos)}) therefore appear to better approximate the EPR spectrum of NiSOD^{ox} (A_{zz} = 69.7 MHz). [9,17,58] When all of the solutions were warmed to room temperature and the EPR spectra were re-recorded at 77 K no signal could be detected above base-line, indicating the decomposition of the Ni^{III} metallopeptides upon warming.

Curiously, comparing {Ni^{III}(SOD^{M1}–Im–DNP)} *vs.* {Ni^{III}(SOD^{M1}–Im–Tos)} it was noted that the superhyperfine coupling constant is *larger* for the metallopeptide with the *weaker* axial imidazole ligand ({Ni^{III}(SOD^{M1}–Im–Tos)}). To gain insight into the origin of this difference we turned our attention to electronic structure calculations. The EPR spectra of the four metallopeptides were simulated using Neese's methodology at the B3LYP level.[54,55] These calculations revealed a surprising aspect of the influence imparted by changing the nature of the axial ligand. We find that as the axial ligand is made less Lewis-basic the orientation of the g_z vector changes. For both Ni^{III}(SOD^{Me}) and Ni^{III}(SOD^{H}) the g_z vector is oriented along the Ni^{III}–N^{imidazole} bond, as would be expected. In Ni^{III}(SOD^{DNP}) the g_z vector becomes more oriented into molecular xy plane. For Ni^{III}(SOD^{Tos}), which has the least Lewis-basic imidazole

donor, the g_z vector becomes oriented along the S-Ni-N^{amine} bond. Furthermore, the SOMO composition switches from a relatively large contribution from the imidazole δ-nitrogen AO in Ni^{III}(SOD^{Me}) and Ni^{III}(SOD^{H}) to negligible contributions from this AO in Ni^{III}(SOD^{DNP}) and Ni^{III}(SOD^{Tos}) (Supporting Information). Therefore, it appears that in {Ni^{III}(SOD^{M1}–Im–DNP)} and {Ni^{III}(SOD^{M1}–Im–Tos)} the observed superhyperfine coupling in g_z appears to be due to the amine nitrogen *not* the imidazole nitrogen.

In a study performed by Brunold and coworkers it was found that variation of the axial imidazole ligand from 2.07 – 2.16 Å (due to outersphere H-bonding interactions) in NiSOD computational models effected a change in the g-values, but not a significant change in superhyperfine coupling.[17] It was reasoned that the increase in the Ni^{III}–N bond length dropped the energy of the SOMO, which increased the anisotropy of the g–tensor *via* mixing of the SOMO with the Ni-based MOs through a spin-orbit coupling mechanism. In contrast, the change in the Ni^{III}–N bond length did not have a dramatic influence on the composition of the SOMO, and thus the superhyperfine coupling constant remained fairly constant as the bond length was changed. We observe something quite different in our systems where the axial ligands themselves are changed, not the axial Ni^{III}–N bond lengths. As the imidazole ligand is changed from a more to a less Lewis–basic ligand we observe a large change in the composition of the AO, as noted above, but not a large change in the relative energetics of the SOMO *vs.* the other filled Ni-based MOs. Therefore orbital mixing *via* a spin-orbit coupling mechanism would be similar for the four metallopeptides studied, resulting in similar g-values across the series. However, because of the changes in the composition of the SOMO we observe larger changes in the computationally derived superhyperfine coupling constants. This is what is observed experimentally.

These observations may help explain why superhyperfine coupling was observed in the oxidized His(1)Gln mutant of NiSOD.[18,27] This Ni^{III} center likely lacks axial Ni^{III}–N ligation yet still displays the characteristic three line splitting in g_z observed for native NiSOD. The above data suggest that the superhyperfine coupling observed in the g_z of NiSOD^{ox}, which has a Ni^{III}–N distance between 2.3 – 2.6 Å, is possibly due to coupling of the unpaired spin with the amine nitrogen not the axial imidazole.

SOD Activity of {Ni(SOD^{M1}–Im–X)} (X = Me, H, DNP, and Tos) Investigated By Stopped-Flow Kinetics

We previously reported that {Ni(SOD^{M1}–Im–H)} is SOD active based on both a simple NBT assay and the xanthine/xanthine oxidase assay.[23,24,68] From the xanthine/xanthine oxidase assay we obtained an IC$_{50}$ = 2(1) × 10^{-7} M for {Ni(SOD^{M1}–Im–H)}.[23] This is less than an order of magnitude poorer than the activity obtained from naturally occurring SODs; Cu/Zn SOD displays an IC$_{50}$ = 4 × 10^{-8} M, or 8 × 10^{-8} M per subunit.[68] The NBT assay also indicated high SOD activity for {Ni(SOD^{M1}–Im–H)}.[22]

Both of the NBT and xanthine/xanthine oxidase assays are indirect methods for monitoring SOD activity; a competition reaction is set up between the SOD mimic and a reporter molecule. The drawback with these methods is it is impossible to know if the SOD mimic is reacting with $O_2^{\bullet-}$ directly (i.e. catalyzing $O_2^{\bullet-}$ disproportionation) or if it is interfering with the $O_2^{\bullet-}$ production, the indicator molecule, or $O_2^{\bullet-}$ itself in a manner not related to $O_2^{\bullet-}$ disproportionation.[69] To circumvent this issue we monitored the direct decomposition of $O_2^{\bullet-}$ using stopped-flow kinetics by monitoring the disappearance of $O_2^{\bullet-}$ at 245 nm (ε = 2250 M^{-1} s^{-1}).

We employed a double mixing stopped flow system to increase the dilution of anhydrous DMSO (the solvent used for solubilizing the KO$_2$ 18-crown-6 salt) into the buffer.[29] This was done for two reasons. One is that by diluting the DMSO in buffer we can better approximate

the situation observed in pure buffer. The second reason is that dilution of the DMSO into an excess of buffer using a double mixing device allows us to minimize any optical disturbances resulting from mixing of the two dissimilar solvents. However, the first 5 ms of the kinetics run beyond the instrument's deadtime still had to be eliminated due to optical disturbances that could not be compensated for by baseline subtraction.

All reactions employed 50 mM NEM buffer at pH = 8.0. The increase in pH from 7.4 to 8.0 was done to slow down the $O_2^{\bullet-}$ self disproportionation reaction, which under these conditions we measure to be $7(1) \times 10^4 \ M^{-1} \ s^{-1}$ (Figure 9). When {Ni(SOD^{M1}–Im–H)} is added to solution we observe a change in the decay kinetics of $O_2^{\bullet-}$ from a second order process to a pseudo-first order process (Figure 9). This is due to the second order catalytic decomposition of $O_2^{\bullet-}$ by {Ni(SOD^{M1}–Im–H)}, which is first order in both reactant (Table 2, Supporting Information). Although the reaction between {Ni(SOD^{M1}–Im–H)} and $O_2^{\bullet-}$ is faster than the self-disproportionation reaction ($k = 7(3) \times 10^7 \ M^{-1} \ s^{-1}$), it is at least one and a half orders of magnitude slower than the reaction observed between $O_2^{\bullet-}$ and NiSOD at this pH ($k_{cat} \sim 1 \times 10^9 \ M^{-1} \ s^{-1}$).[27] These data therefore demonstrate that {Ni(SOD^{M1}–Im–H)} is a poorer catalyst than one would have concluded from the xanthine/xanthine oxidase assay; using the xanthine/ xanthine oxidase assay the activity of {Ni(SOD^{M1}–Im–H)} was overestimated by over an order of magnitude.

The $O_2^{\bullet-}$ disproportionation kinetics of the other three metallopeptides were also investigated using stopped-flow kinetics. We found that all three of the *N*–substituted imidazole substituted metallopeptides are capable of facilitating the catalytic disproportionation of $O_2^{\bullet-}$. The metallopeptide with the most electron rich Ni^{III}-center, {Ni^{III}(SOD^{M1}–Im–Me)}, affords the slowest pseudo-first order $O_2^{\bullet-}$ degradation kinetics of the four metallopeptides investigated ($k = 6(1) \times 10^6 \ M^{-1} \ s^{-1}$). In contrast, both {Ni^{III}(SOD^{M1}–Im–DNP)} and {Ni^{III}(SOD^{M1}–Im– Tos)} display $O_2^{\bullet-}$ degradation kinetics that are faster than {Ni^{III}(SOD^{M1}–Im–H)} with $k = 4 (2) \times 10^8 \ M^{-1} \ s^{-1}$ and $6(2) \times 10^8 \ M^{-1} \ s^{-1}$, respectively.

Summary and Conclusion

In this study we have utilized unnatural amino acids in metallopeptide based NiSOD mimics to probe the influence of a H-bonding network in the metalloenzyme. It was reasoned that we could approximate the electronic consequence of this *structural* feature in the metalloenzyme by altering the ligand based electronics of the axial His(1) imidazole donor by appending electron donating and withdrawing groups to the imidazole ε-nitrogen. In essence, it was reasoned that by utilizing less Lewis-basic imidazole donors the electronic properties of the nickel center in NiSOD could be approximated.

In all cases, we did not observe significant influences on the structure and properties of the reduced Ni^{II} forms of the metallopeptides as the His(1) imidazole was modified. This should be expected because the imidazole does not coordinate to the reduced Ni^{II} center. In contrast, significant differences in the spectroscopic and reactivity properties of the oxidized Ni^{III} metallopeptides were observed as the imidazole ligand electronics were changed. We observe that as the imidazole ligand is made less Lewis-basic the metallopeptide based model begins to better approximate the properties of the metalloenzyme; the EPR properties, N-Ni-S stretching frequencies, and the resulting SOD activity all become similar to the metalloenzyme as the axial imidazole donor is made less Lewis basic. We note that some stabilizing interaction to the Ni-center is required as removal of this ligand (e.g. the His to Ala modification) produces a catalytically inactive SOD who's Ni^{III} state cannot be stabilized for study.[18] Therefore subtle changes to the axial ligand translate into profound differences in SOD activity effected by these NiSOD metallopeptide mimics; too strong of an axial ligand *and* too weak of an axial ligand will both dramatically hinder (if not out-right shut-down) SOD activity.

The likely explanations for the influence of the axial imidazole ligand are both rooted in electron transfer to and from the Ni-center. The metallopeptide with the least Lewis basic imidazole donor $\{Ni(SOD^{M1}–Im–Tos)\}$ has a redox potential that is nearly identical to the pH 7 mid-point $O_2^{\bullet-}$ oxidation/reduction potentials.[66] It is therefore electrochemically optimized to perform SOD chemistry under near physiological conditions; neither the oxidation nor reduction reaction will slow down the overall disproportionation reaction. In contrast, the metallopeptide with the most Lewis basic imidazole donor, $\{Ni(SOD^{M1}–Im–Me)\}$, has a Ni^{II}/Ni^{III} redox potential that is nearly 300 mV more negative than the mid-point of the superoxide oxidation/reduction potentials. Therefore, the reduction of superoxide by $\{Ni^{II}(SOD^{M1}–Im–Me)\}$ will dramatically retard the overall rate of $O_2^{\bullet-}$ disproportionation by $\{Ni(SOD^{M1}–Im–Me)\}$. There are also significant changes in Ni-ligand bond strengths as the imidazole ligand's electronics are changed. This will likely influence the rate of SOD kinetics for this metalloenzyme as this will change the inner-sphere reorganization energy (λ_i) from metallopeptide to metallopeptide. It is highly likely that both of these factors are combining in a serendipitous manner to allow for efficient catalytic SOD activity in $\{Ni(SOD^{M1}–Im–Tos)\}$ and $\{Ni(SOD^{M1}–Im–DNP)\}$. NiSOD itself, with the limited number of naturally occurring amino-acid residues available, utilizes the His(1)…Glu(17)…Arg(47) H-bonding network to effectively "reduce" the Lewis-basicity of the imidazole ligand (from the standpoint of the Ni^{III}–center). Thus, NiSOD likely optimizes its electron transfer properties through a rack/entatic state type mechanism.[18,70–72]

Supplementary Material

Refer to Web version on PubMed Central for supplementary material.

Acknowledgments
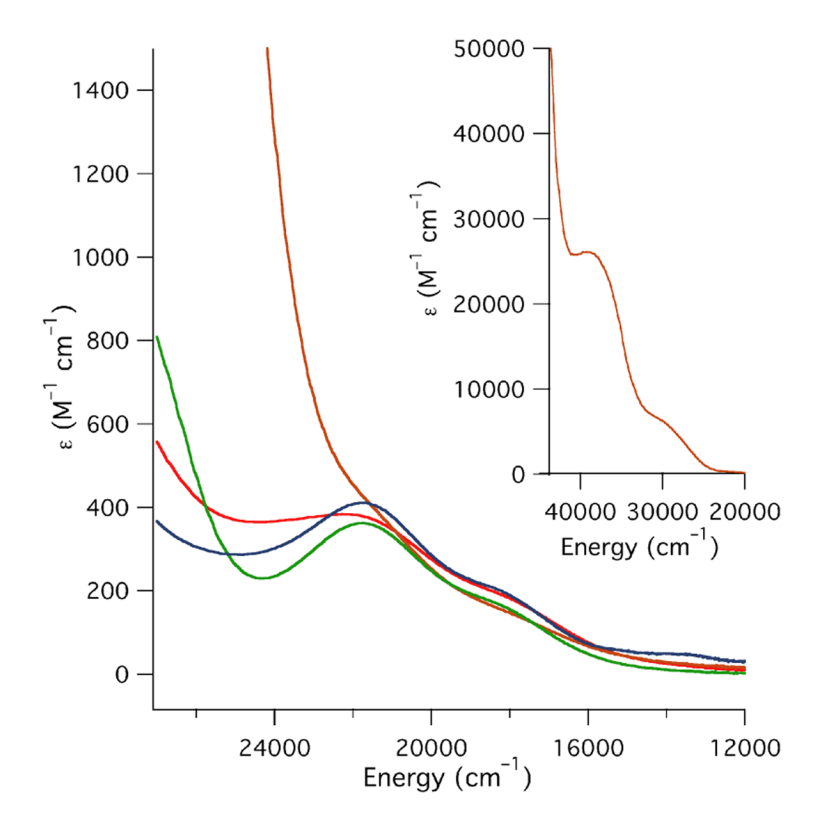
References

1. Bai KVK, Azeez S. Adv Plant Physiol 2006;9:87–100.

2. Cabelli DE, Riley D, Rodriguez JA, Valentine JS, Zhu H. Biomimetic Oxid Catal Transition Met Complexes 2000:461–508.

3. Fridovich I. Annu Rev Biochem 1995;64:97–112. [PubMed: 7574505]

4. Stallings WC, Metzger AL, Pattridge KA, Fee JA, Ludwig ML. Free Radical Res Commun 1991;12–13:259–68.

5. Fridovich I. Encycl Biol Chem 2004;4:135–138.

6. Grove LE, Brunold TC. Comments Inorg Chem 2008;29:134–168.

7. Miller AF. Acc Chem Res 2008;41:501–510. [PubMed: 18376853]

8. Bryngelson PA, Maroney MJ. Met Ions Life Sci 2007;2:417–443.

9. Youn HD, Kim EJ, Roe JH, Hah YC, Kang SO. Biochem J 1996;318:889–896. [PubMed: 8836134]

10. Lee JW, Roe JH, Kang SO. Methods Enzymol 2002;349:90–101. [PubMed: 11912934]

11. Youn HD, Youn H, Lee JW, Yim YI, Lee JK, Hah YC, Kang SO. Arch Biochem Biophys 1996;334:341–348. [PubMed: 8900409]

12. Palenik B, Brahamsha B, Larimer FW, Land M, Hauser L, Chain P, Lamerdin J, Regala W, Allen EE, McCarren J, Paulsen I, Dufresne A, Partensky F, Webb EA, Waterbury J. Nature 2003;424:1037–1042. [PubMed: 12917641]

13. Dupont CL, Neupane K, Shearer J, Palenik B. Environ Microbiol 2008;10:1831–1843. [PubMed: 18412551]
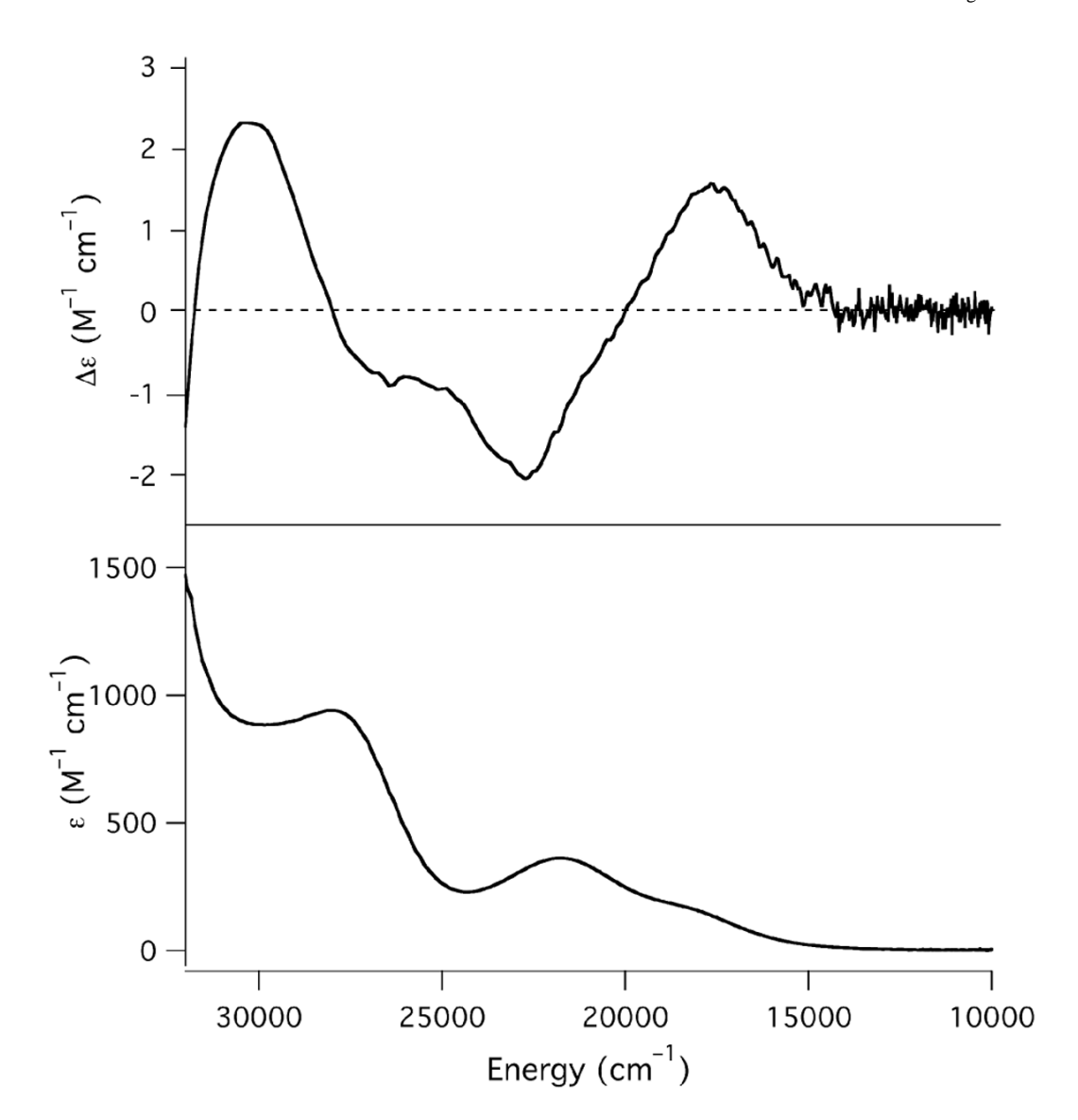
14. Kurtz DM Jr. Chemtracts 2004;17:212–217.

15. Barondeau DP, Kassmann CJ, Bruns CK, Tainer JA, Getzoff ED. Biochemistry 2004;43:8038–8047. [PubMed: 15209499]

16. Wuerges J, Lee JW, Yim YI, Yim HS, Kang SO, Carugo KD. Proc Natl Acad Sci U S A 2004;101:8569–8574. [PubMed: 15173586]

17. Fiedler AT, Bryngelson PA, Maroney MJ, Brunold TC. J Am Chem Soc 2005;127:5449–5462. [PubMed: 15826182]

18. Neupane KP, Gearty K, Francis A, Shearer J. J Am Chem Soc 2007;129:14605–14618. [PubMed: 17985883]

19. Kruger HJ, Holm RH. J Am Chem Soc 1990;112:2955–63.

20. Machida R, Kimura E, Kushi Y. Inorg Chem 1986;25:3461–6.

21. Orpen AG, Brammer L, Allen FH, Kennard O, Watson DG, Taylor R. J Chem Soc, Dalton Trans 1989:S1–S83.

22. Pelmenschikov V, Siegbahn PEM. J Am Chem Soc 2006;128:7466–7475. [PubMed: 16756300]

23. Neupane KP, Shearer J. Inorg Chem 2006;45:10552–10566. [PubMed: 17173410]

24. Shearer J, Long LM. Inorg Chem 2006;45:2358–2360. [PubMed: 16529443]

25. Schmidt M, Zahn S, Carella M, Ohlenschlaeger O, Goerlach M, Kothe E, Weston J. ChemBioChem 2008;9:2135–2146. [PubMed: 18690655]

26. Tietze D, Breitzke H, Imhof D, Kothe E, Weston J, Buntkowsky G. Chem--Eur J 2009;15:517–523.

27. Bryngelson PA, Arobo SE, Pinkham JL, Cabelli DE, Maroney MJ. J Am Chem Soc 2004;126:460–461. [PubMed: 14719931]

28. Ellman GL. Arch Biochem Biophys 1958;74:443–50. [PubMed: 13534673]

29. Riley DP, Rivers WJ, Weiss RH. Anal Biochem 1991;196:344–9. [PubMed: 1663709]

30. Weiss RH, Flickinger AG, Rivers WJ, Hardy MM, Aston KW, Ryan US, Riley DP. J Biol Chem 1993;268:23049–54. [PubMed: 8226820]

31. Goldstein S, Fridovich I, Czapski G. Free Radical Biol Med 2006;41:937–941. [PubMed: 16934676]

32. Lehnert N, Tuczek F. Inorg Chem 1999;38:1659–1670. [PubMed: 11670933]

33. Scarrow, RC. EXAFS123. Haverford College; Haverford, PA: 2005.

34. Ankudinov AL, Ravel B, Rehr JJ, Conradson SD. Phys Rev B: Condens Matter Mater Phys 1998;58:7565–7576.

35. Ankudinov AL, Bouldin CE, Rehr JJ, Sims J, Hung H. Phys Rev B: Condens Matter Mater Phys 2002;65:104107/1–104107/11.

36. Neese, F. ORCA, An Ab Initio, Density Functional, and Semiempirical Program Package. Vol. 2.6.35. Universitat Bonn; Bonn, Germany: 2008.

37. Vosko SH, Wilk L, Nusair M. Can J Phys 1980;58:1200–11.

38. Becke AD. J Chem Phys 1986;84:4524–9.

39. Becke AD. Phys Rev A: Gen Phys 1988;38:3098–100.

40. Becke AD. J Chem Phys 1988;88:1053–62.

41. Perdew JP. Phys Rev B: Condens Matter Mater Phys 1986;33:8822–8824.

42. Perdew JP. Phys Rev B: Condens Matter Mater Phys 1986;34:7406.

43. Schaefer A, Horn H, Ahlrichs R. J Chem Phys 1992;97:2571–7.

44. Ahlrichs, R.; coworkers *unpublished.*

45. Neese, F. unpublished results.

46. Balabanov NB, Peterson KA. J Chem Phys 2005;123:64107. [PubMed: 16122300]

47. Woon DE, Dunning TH Jr. J Chem Phys 1993;98:1358–71.

48. Becke AD. J Chem Phys 1993;98:5648–52.

49. Lee C, Yang W, Parr RG. Phys Rev B: Condens Matter Mater Phys 1988;37:785–9.

50. Gaussian 03, Revision C.02. Gaussian, Inc; Wallingford CT: 2004.

51. Praneeth VKK, Naether C, Peters G, Lehnert N. Inorg Chem 2006;45:2795–2811. [PubMed: 16562937]

52. Allouche A, Pourcin J. Spectrochim Acta, Part A 1993;49A:571–80.

53. Peterson MR, McIntosh DF. QCPE :576.

54. Neese F. J Chem Phys 2001;115:11080–11096.

55. Neese F. Curr Opin Chem Biol 2003;7:125–135. [PubMed: 12547437]

56. Kutzelnigg, W.; Fleischer, U.; Schindler, M. The IGLO-Method: Ab-initio Calculation and Interpretation of NMR Chemical Shifts and Magnetic Susceptibilities. Vol. 213. Springer Verlag; Berlin/Heidelberg, Germany: 1991.

57. Colpas GJ, Maroney MJ, Bagyinka C, Kumar M, Willis WS, Suib SL, Mascharak PK, Baidya N. Inorg Chem 1991;30:920–8.

58. Choudhury SB, Lee JW, Davidson G, Yim YI, Bose K, Sharma ML, Kang SO, Cabelli DE, Maroney MJ. Biochemistry 1999;38:3744–3752. [PubMed: 10090763]

59. Hu Y, Hu N. J Phys Chem B 2008;112:9523–9531. [PubMed: 18616316]

60. Wang L, Waldeck DH. J Phys Chem C 2008;112:1351–1356.

61. Sumner JJ, Weber KS, Hockett LA, Creager SE. J Phys Chem B 2000;104:7449–7454.

62. Sumner JJ, Creager SE. J Phys Chem B 2001;105:8739–8745.

63. Herbst RW, Guce A, Bryngelson PA, Higgins KA, Ryan KC, Cabelli DE, Garman SC, Maroney MJ. Biochemistry 2009;48:3354–3369. [PubMed: 19183068]

64. Sawyer DT, Valentine JS. Acc Chem Res 1981;14:393–400.

65. Westre TE, Kennepohl P, DeWitt JG, Hedman B, Hodgson KO, Solomon EI. J Am Chem Soc 1997;119:6297–6314.

66. Roe AL, Schneider DJ, Mayer RJ, Pyrz JW, Widom J, Que L Jr. J Am Chem Soc 1984;106:1676–81.

67. Fiedler AT, Brunold TC. Inorg Chem 2007;46:8511–8523. [PubMed: 17305331]

68. Tabbi G, Driessen WL, Reedijk J, Bonomo RP, Veldman N, Spek AL. Inorg Chem 1997;36:1168–1175. [PubMed: 11669684]

69. Riley DP. Chem Rev 1999;99:2573–2587. [PubMed: 11749493]

70. Malmstrom BG. Eur J Biochem 1994;223:711–8. [PubMed: 8055947]

71. Williams RJP. Eur J Biochem 1995;234:363–81. [PubMed: 8536678]

72. Vallee BL, Williams RJ. Proc Natl Acad Sci U S A 1968;59:498–505. [PubMed: 5238980]

Figure 1.
Electronic absorption spectra of {Ni^{II}(SOD^{M1}–Im–H)} (blue trace), {Ni^{II}(SOD^{M1}–Im–Me)} (green trace), {Ni^{II}(SOD^{M1}–Im–Tos)} (red trace), and {Ni^{II}(SOD^{M1}–Im–DNP)} (orange trace). Inset depicts the expanded spectrum of {Ni^{II}(SOD^{M1}–Im–DNP)}.

Figure 2.
Electronic absorption (bottom) and CD spectrum (top) of {Ni^{II}(SOD^{M1}–Im–Me)}.
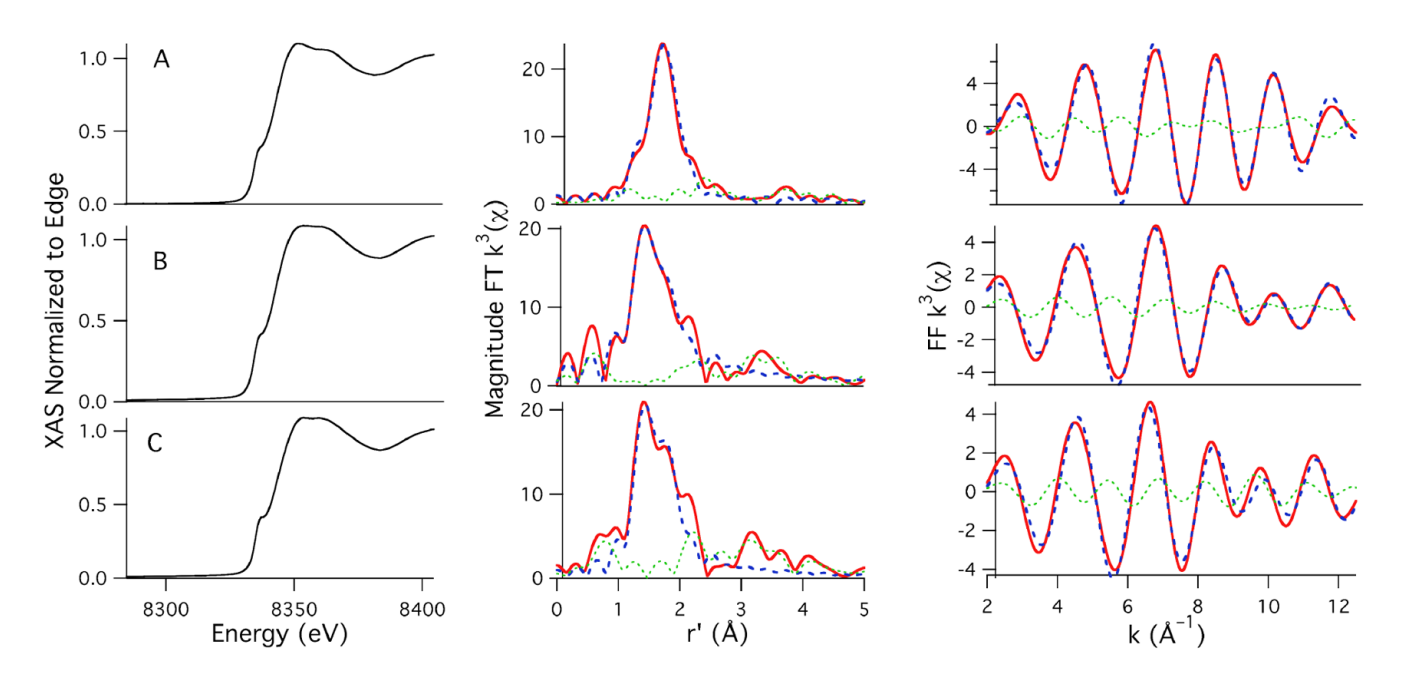
Figure 3.
Ni K-edge X-ray absorption data for {Ni^{II}(SOD^{M1}–Im–Me)} (A), {Ni^{II}(SOD^{M1}–Im–Tos)} (B), and {Ni^{II}(SOD^{M1}–Im–DNP)} (C). The left portion of the figure contains the edge spectra, which display prominent Ni(1s → 4p$_z$) transitions indicative of square-planar Ni^{II}, the middle contains the FT k^3 EXAFS data, and the left displays the FF k^3 EXAFS data. Experimental data are shown in red, simulations to the data are shown in dashed blue, and the difference spectrum is shown in green. {Ni^{II}(SOD^{M1}–Im–Me)} was obtained at a concentration of ~3 mM, while {Ni^{II}(SOD^{M1}–Im–Tos)} and {Ni^{II}(SOD^{M1}–Im–DNP)} were recorded at submillimolar concentrations due to solubility issues.
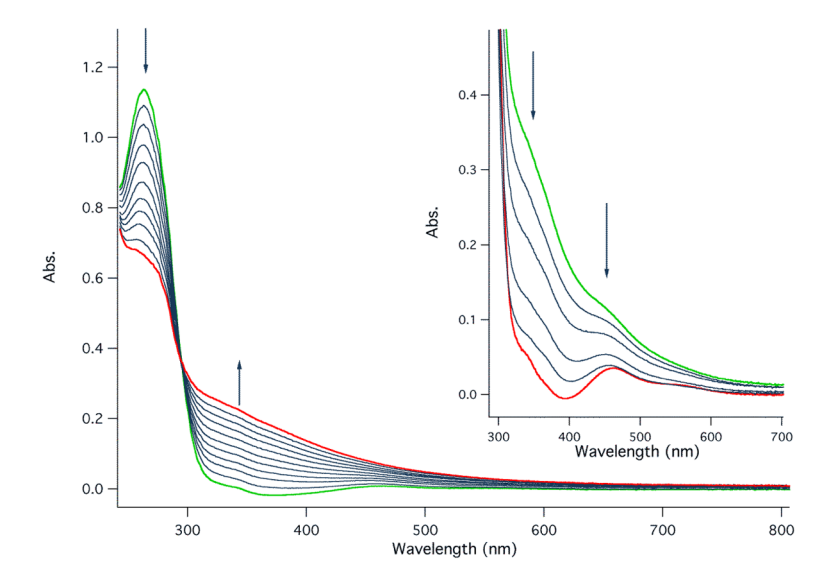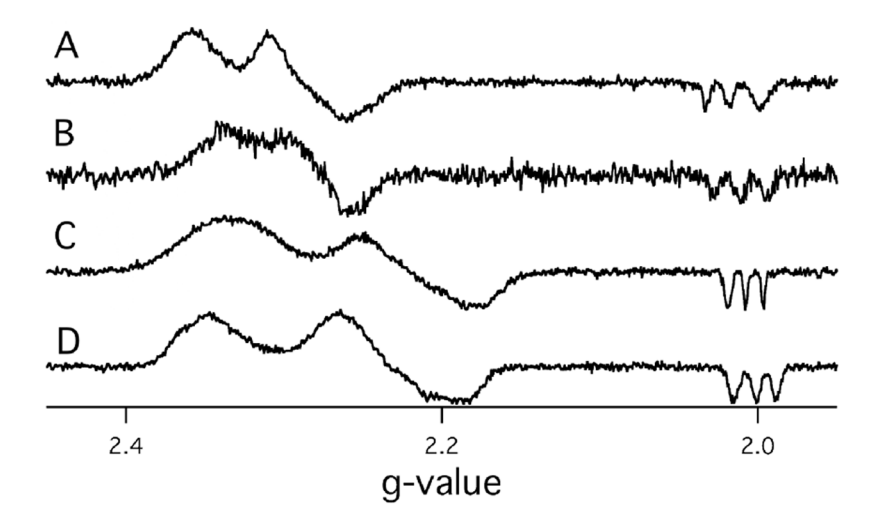
Figure 4.
Oxidation of {Ni^{II}(SOD^{M1}–Im–Me)} promoted by the addition of one equivalent of KMnO$_4$ to pH 7.4 solutions of {Ni^{II}(SOD^{M1}–Im–Me)} in 0.1 eq. aliquots. The green trace is the beginning point of the titration and the red trace is the end point. The inset depicts the tail-end of the ascorbate effected reduction of oxidized {Ni^{III}(SOD^{M1}–Im–Me)} by the addition of ascorbate in aliquots of 0.05 reducing eq. at pH 7.4. The green trace is the "beginning point" of the titration and the red trace is the end point.

Figure 5.
EPR spectra (77 K) of {Ni^{III}(SOD^{M1}–Im–Me)} (A), {Ni^{III}(SOD^{M1}–Im–H)} (B), {Ni^{III}(SOD^{M1}–Im–DNP)} (C), and {Ni^{III}(SOD^{M1}–Im–Tos)} (D).
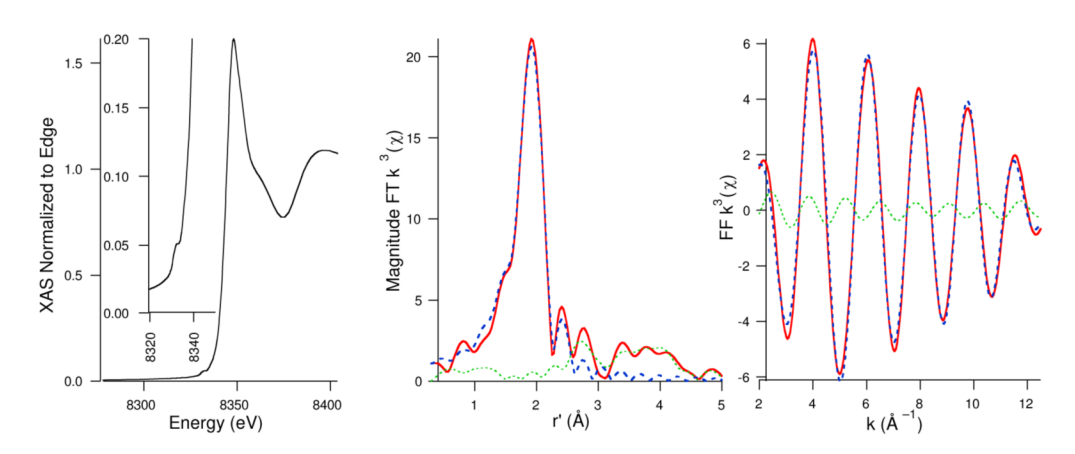
Figure 6.
Ni K-edge X-ray absorption data for I_2 generated {$Ni^{III}(SOD^{M1}$–Im–Me)} (concentration ~ 3 mM). Experimental data are shown in red, simulations to the data are shown in dashed blue, and the difference spectrum is shown in green. The left figure shows the XANES region of the XAS, the middle figure shows the FT k^3 EXAFS, and the right figure shows the FF k^3 EXAFS. The inset presented in the XANES panel displays an expansion of the Ni(1s → 3d) transition.
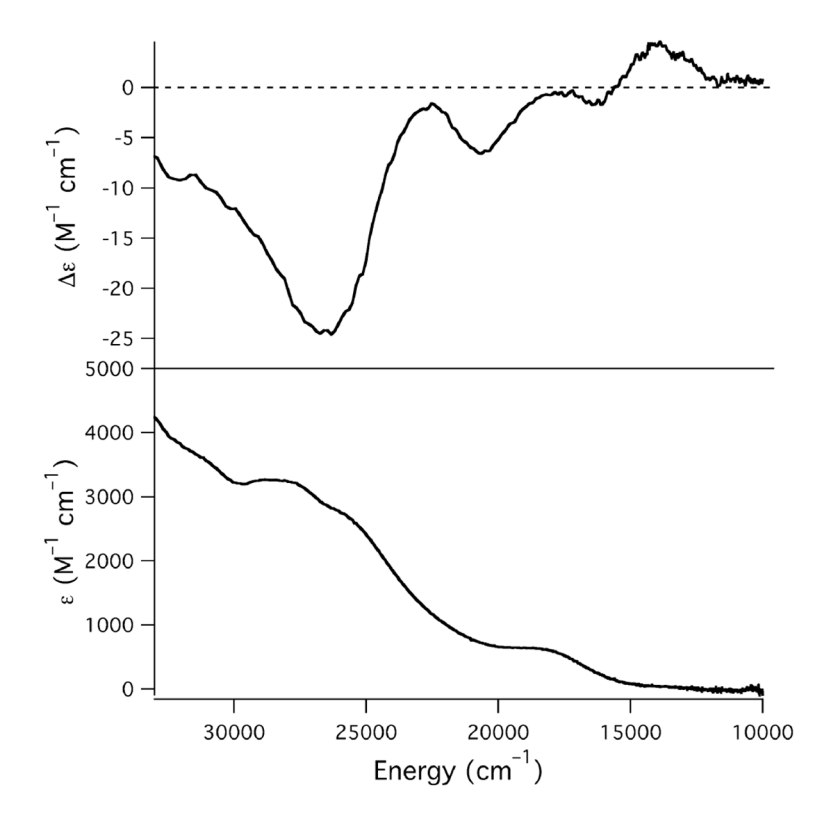
Figure 7.
Electronic absorption spectrum (bottom) and CD spectrum (top) of {Ni^{III}(SOD^{M1}–Im–Me)}.
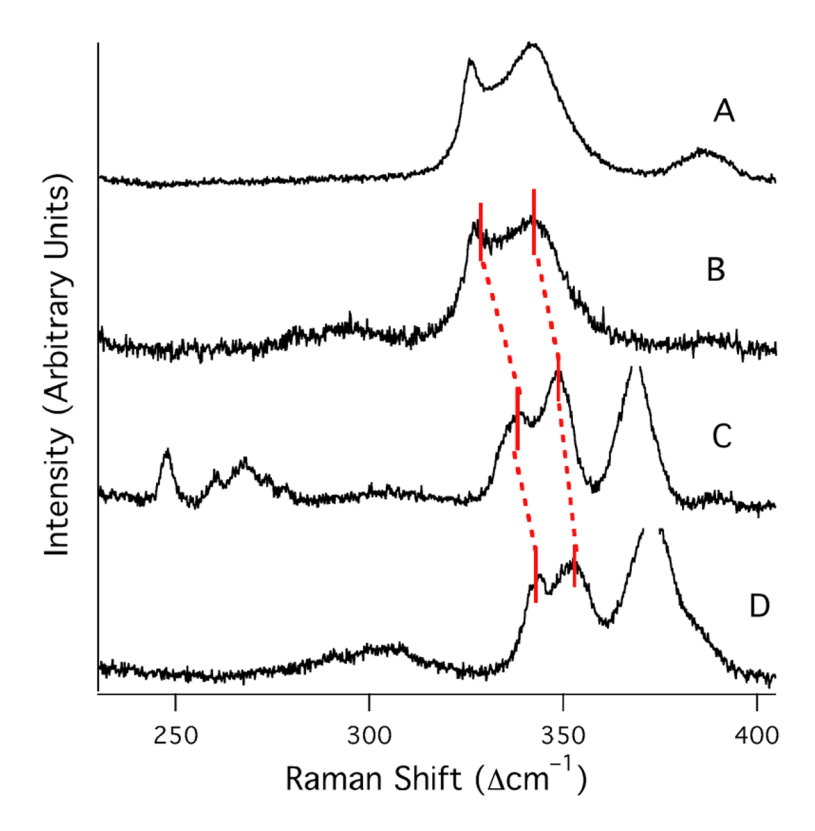
Figure 8.
Resonance Raman spectra of {$Ni^{III}(SOD^{M1}–Im–Me)$} (A and B, recorded at room temperature and 77 K, respectively), {$Ni^{III}(SOD^{M1}–Im–DNP)$} (C; 77 K), and {$Ni^{III}(SOD^{M1}–Im–Tos)$} (D; 77 K) following 405 nm excitation. The symmetric N-Ni-S stretching modes are highlighted in red.
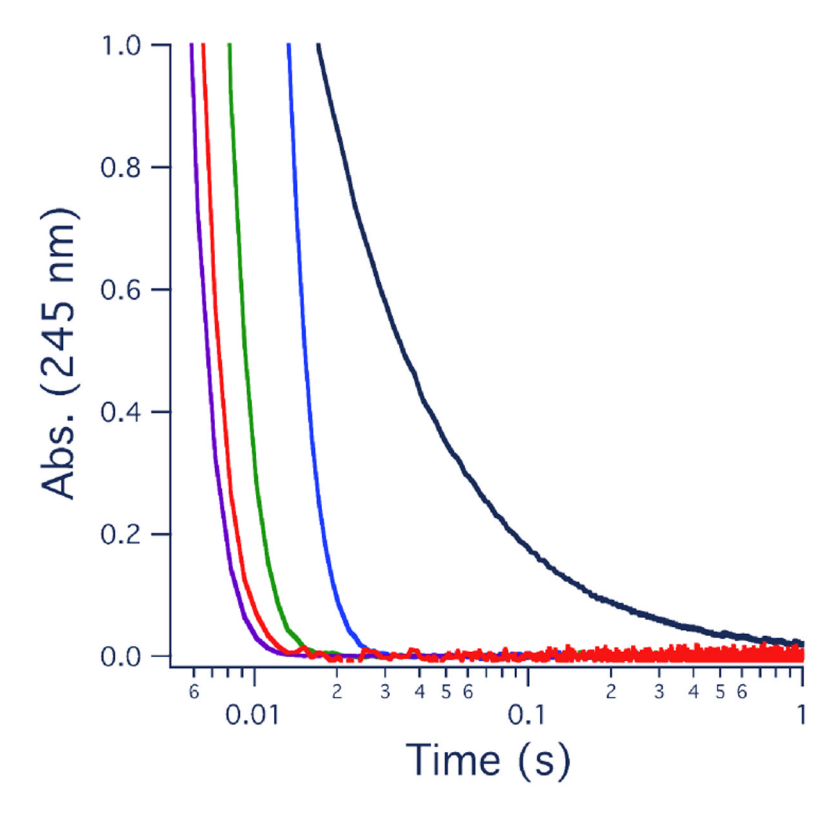
Figure 9.
Decay trace for the disproportionation of 50 mM KO_2 (18-c-6 salt) {Ni(SOD^{M1}–Im–X)} (pH 8.0 T = 24.7 °C). The black trace is the KO_2 self-disproportionation, the blue trace is {Ni (SOD^{M1}–Im–Me)} (60 μM), the green trace is {Ni(SOD^{M1}–Im–H)} (12 μM), the red trace is {Ni(SOD^{M1}–Im–DNP)} (2.0 μM), and the purple blue trace is {Ni(SOD^{M1}–Im–Tos)} (1.0 μM).

Scheme 1.

Chart 1.

Table 1

Electronic absorption, circular dichroism, electrochemical data for {Ni^{II}(SOD^{M1}–Im–X)} (X = Me, DNP, and Tos) and {Ni^{III}(SOD^{M1}–Im–Me)}.

	UV/Vis (λ_{max} (cm^{-1}) (ε (M^{-1} cm^{-1})	CD (λ (cm^{-1}) ($\Delta\varepsilon$ (M^{-1} cm^{-1})	E (V vs. Ag/Ag$^+$)
{Ni^{II}(SOD^{M1}–Im–Me)}	18,050 (160, sh)	17,670 (1.60)	282(4)
	21,690 (360)	22,940 (–2.04)	
	27,400 (940)	30,300 (2.31)	
{Ni^{II}(SOD^{M1}–Im–DNP)}	18,110 (150, sh)	18,797 (–2.32)	470(10)
	21,560 (410, sh)	21,740 (6.00)	
	38,127 (25,700)	26,880 (70.7)	
		29,940 (63.4)	
{Ni^{II}(SOD^{M1}–Im–Tos)}	18,110 (180, sh)	17,185 (1.90)	598(5)
	21,730 (405, sh)	22,420 (–2.95)	
		30,490 (5.33)	
{Ni^{III}(SOD^{M1}–Im–Me)}	18,210 (740)	13,950 (4.19)	nd.[a]
	25,575 (sh)	16,445 (–1.73)	
	28,575 (3,260)	20,660 (–6.59)	

[a]
nd. = not determined

Table 2

Ni K-edge X-ray absorption refinement parameters for {Ni^{II}(SOD^{M1}–Im–X)} (X = Me, DNP, and Tos) and {Ni^{III}(SOD^{M1}–Im–Me)}.

	{Ni^{II}(SOD^{M1}–Im–Me)}	{Ni^{II}(SOD^{M1}–Im–Tos)}	{Ni^{II}(SOD^{M1}–Im–DNP)}	{Ni^{III}(SOD^{M1}–Im–Me)}
Edge Energy (eV)	8340.2(4)	8340.3(2)	8340.2(1)	8342.5(1)
Pre-edge Peak 1 (eV)	8332.7(2)	8332.4(2)	8332.5(2)	8334.1(1)
intensity[a]	0.03	0.026	0.028	0.079
Pre-edge Peak 2 (eV)	8337.9(2)	8338.0(1)	8338.1(1)	----
intensity[a]	0.42	0.43	0.46	
E_o (eV)	8343.5	8343.2	8343.2	8344.1
N Shell				
n	2	2	2	3
r (Å)	1.91(1)	1.87(2)	1.89(1)	1.894(3)
σ^2 (Å^2)	0.0026(3)	0.0029(6)	0.0028(5)	0.0037(2)
S Shell				
n	2	2	2	2
r (Å)	2.182(1)	2.174(2)	2.179(2)	2.174(1)
σ^2 (Å^2)	0.0022(8)	0.0034(4)	0.0027(3)	0.0029(3)
GOF[b]	0.31	0.68	0.54	0.33

[a] intensity relative to the edge with an uncertainty of ~ ±5%.

[b] GOF = $R[n\{idp\}/(n\{idp\} - n\{p\})]1/2$; R = ave[(data-simulation)/*esd(data)*; *n(p)= number of varied paramters; n(idp) = 2(rmax−rmin)(kmax−kmin)/π*

Table 3

EPR results for {Ni^{III}(SOD^{M1}–Im–Me)}, {Ni^{III}(SOD^{M1}–Im–H)}, {Ni^{III}(SOD^{M1}–Im–Tos)}, {Ni^{III}(SOD^{M1}–Im–DNP)}. Calculated results were obtained using the B3LYP functional by solving the CP-SCF equations.

| | g$_x$ (A$_{xx}$ MHz) | | g$_y$ (A$_{yy}$ MHz) | | g$_z$ (A$_{zz}$ MHz) | |
	exp	calcd.	exp	calcd.	exp	calcd.
{Ni^{III}(SOD^{M1}–Im–Me)}	2.36 (nd)	2.284 (69.2)	2.29 (nd)	2.260 (55.3)	2.02 (83)	2.040 (74.0)
{Ni^{III}(SOD^{M1}–Im–H)}	2.33 (nd)	2.288 (69.5)	2.27 (nd)	2.263 (55.2)	2.01 (81)	2.032 (73.9)
{Ni^{III}(SOD^{M1}–Im–DNP)}	2.33 (nd)	2.282 (59.9)	2.22 (nd)	2.169 (48.2)	2.00 (55)	2.048 (51.3)
{Ni^{III}(SOD^{M1}–Im–Tos)}	2.33 (nd)	2.286 (57.2)	2.24 (nd)	2.206 (46.9)	2.00 (67)	2.045 (65.7)

Table 4

Resonance Raman derived Ni–S force constants and vibrational modes for $\{Ni^{III}(SOD^{M1}–Im–X)\}$ (X = Me, DNP and Tos).

	exp. v (cm^{-1})	calcd. v (cm^{-1})	normal-mode description	f (mdyn Å^{-1})
$\{Ni^{III}(SOD^{M1}–Im–Me)\}$	323	325	$S^a{\leftarrow}Ni + Ni{\rightarrow}N^{amide}$	Ni–S^a: 1.31
	343	340	$S^b{\leftarrow}Ni + Ni{\rightarrow}N^{amine}$	Ni–S^b: 1.54
	388	386	$S^a{\leftarrow}Ni - Ni{\rightarrow}N^{amine}$	
$\{Ni^{III}(SOD^{M1}–Im–DNP)\}$	338	341	$S^a{\leftarrow}Ni + Ni{\rightarrow}N^{amide}$	Ni–S^a: 1.47
	349	349	$S^b{\leftarrow}Ni + Ni{\rightarrow}N^{amine}$	Ni–S^b: 1.69
$\{Ni^{III}(SOD^{M1}–Im–Tos)\}$	343	345	$S^a{\leftarrow}Ni + Ni{\rightarrow}N^{amide}$	Ni–S^a: 1.51
	352	350	$S^b{\leftarrow}Ni + Ni{\rightarrow}N^{amine}$	Ni–S^b: 1.70

[a] cysteinate *trans* to the amide nitrogen.

[b] cysteinate *trans* to the amine nitrogen.